Modeling, design, fabrication, and testing of a fiber Bragg grating strain sensor array

Abdeq M. Abdi, Shigeru Suzuki, Axel Schülzgen, and Alan R. Kost

The modeling, design, simulation, fabrication, calibration, and testing of a three-element, 15.3 cm fiber Bragg grating strain sensor array with the coherent optical frequency domain reflectometry (C-OFDR) interrogation technique are demonstrated. The fiber Bragg grating array (FBGA) is initially simulated using in-house software that incorporates transfer matrices. Compared to the previous techniques used, the transfer matrix method allows a systemwide approach to modeling the FBGA–C-OFDR system. Once designed and simulated, the FBGA system design is then imprinted into the core of a boron–germanium codoped photosensitive fiber using the phase mask technique. A fiber optic Fabry–Perot interferometric (FPI) strain gauge calibrator is then used to determine the strain gauge factor of a single fiber Bragg grating (FBG), and the results are used on the FBGA. The FPI strain gauge calibrator offers nondestructive testing of the FBG. To test the system, the FBGA is then attached to a 75 cm cantilever beam and interrogated using an incremental tunable laser. Electric strain gauges (ESGs) are then used to independently verify the strain measurements with the FBGA at various displacements of the cantilever beam. The results show that the peak strain error is 18% with respect to ESG results. In addition, good agreement is shown between the simulation and the experimental results.

OCIS codes: 060.2370, 070.6020.

1. Introduction

Various methods have been used to simulate the interrogation of a fiber Bragg grating array (FBGA) system with coherent optical frequency domain reflectometry (C-OFDR). Froggatt *et al.*[1] conducted an analysis of the demodulation of a FBGA with C-OFDR interrogation using a variation of the coupled-mode theory. The analysis showed that for a weakly guided and low-reflectivity FBGA system (FBGA plus a reference reflector), the Fourier transform of a C-OFDR signal gives the positional information of each fiber Bragg grating (FBG) in the array, and a narrow inverse Fourier transform at selected positions within this Fourier transform can then be used to recover the wavelength spectrum of a particular FBG. Childers *et al.*[2] used the Fourier transform of a sinusoidal phase grating to approximate the FBG as a sinc function and then summed multiple phase-shifted sinc functions plus the contribution from a reference reflector to model the FBGA system. Duncan *et al.*[3] approximated the interference between the reference reflector and a low-reflectivity FBG using the two-beam interference method and then summed the contribution from each FBG in the array to model the FBGA system.

In this work we demonstrate the modeling–testing cycle of a FBGA–C-OFDR system with the aid of the transfer matrix approach. The transfer matrix method allows a systemwide approach to modeling the FBGA–C-OFDR system.[4] An elemental transfer matrix represents the optical and geometrical characteristics of a single element in the FBGA system. The response of the entire FBGA system is then determined simply by multiplying all the elemental transfer matrices in the proper order. The advantage of this approach is that any optical device can be incorporated efficiently if its transfer matrix is known. Unlike previous techniques, higher interferences will also be taken into account, and the reflectance of the FBGA–C-OFDR system can be determined directly. In this work higher-order interferences will be defined as the interference resulting from a multiple pass through the FBGA system and interference between the beats. It is possible for the cavity interferences to superimpose onto FBG-reflector

A. M. Abdi (abdeqa@aim.com) is with Saada Optical, LLC, 4139 Chouteau Avenue, Saint Louis, Missouri 63110, USA. S. Suzuki, A. Schülzgen, and A. R. Kost are with the College of Optical Sciences, University of Arizona, 1630 East University Boulevard, Tucson, Arizona 85721, USA.

Received 19 September 2006; accepted 7 January 2007; posted 22 January 2007 (Doc. ID 75213); published 23 April 2007.

0003-6935/07/142563-12$15.00/0

interferences when their corresponding beat frequencies are equal, resulting in the distortion of the recovered FBG spectra. Several techniques have been implemented to eliminate this distortion. The first technique is to reduce the reflectance of the FBGs to a level that minimizes the cavity interferences. The second method is to downshift the cavity interferences to a lower-frequency band.[5,6] A third technique, simulated in a prior paper,[4] is to actively subtract the cavity interferences directly from the overall FBGA system interference signal. Finally, in this work, the cavity interferences will be taken into account by precisely designing the FBGA system such that the cavity interferences and the FBG-reflector interferences do not overlap.

2. Fiber Bragg Grating Strain Sensor Array

A. Fiber Bragg Gratings

A FBG is essentially an optical fiber with a periodically perturbed refractive index core. The perturbed refractive index core couples optical energy between the modes of an optical fiber. In a single-mode optical fiber operating below cutoff, the optical energy is coupled between two counterpropagating LP_{01} modes for a reflective-type FBG. As shown in Fig. 1, if a reflective-type FBG is illuminated by a broadband source or scanned by a tunable laser source, a narrow band will be reflected in the direction of the source, where the center of this narrow band is the Bragg wavelength, λ_B. The coupled-mode equations can be used to describe the interactions between the modes in a perturbed refractive index. For a uniform (sinusoidal index perturbation) FBG, the coupled-mode equations are given by[7]

$$\frac{\partial E_i(z)}{\partial z} = -j\kappa E_r(z)e^{-j2\delta z},$$

$$\frac{\partial E_r(z)}{\partial z} = j\kappa E_i(z)e^{-j2\delta z}, \tag{1}$$

where $E_i(z)$, $E_r(z)$, κ, and δ are the forward-propagating field, counterpropagating field, coupling constant, and phase-matching condition, respectively. The phase-matching condition relates the magnitude of the propagation vector of the two modes with the magnitude of the grating vector. The phase-matching condition is given by

$$\delta = \frac{1}{2}(2\beta - K),$$

$$= 2\pi n\left(\frac{1}{\lambda} - \frac{1}{\lambda_B}\right), \tag{2}$$

where β is the magnitude of the propagation vector, K is the magnitude of the grating vector, n is the effective refractive index, and λ is the operating wavelength. From Eq. (1), for specific coupling constant κ, peak coupling occurs between the counterpropagation modes when the phase-matching condition is satisfied ($\delta = 0$); this occurs when the operating wavelength is equal to the Bragg wavelength, where the Bragg wavelength is directly related to the period of the grating, Λ, and the effective refractive index

$$\lambda_B = 2n\Lambda. \tag{3}$$

If there is no input from the right of the grating, the input and output relationship of the grating can be related through the transfer matrix $\mathbf{T}$:

$$\begin{bmatrix} E_i(0) \\ E_r(0) \end{bmatrix} = [T]\begin{bmatrix} E_i(l) \\ 0 \end{bmatrix}, \tag{4}$$

where l is the length of the grating. Solving the coupled-mode equations, the transfer matrix for a uniform reflective-type FBG is given by[7]

$$T = \begin{bmatrix} \cosh(\alpha l) - \dfrac{j\delta \sinh(\alpha l)}{\alpha} & -j\dfrac{\kappa \sinh(\alpha l)}{\alpha} \\ j\dfrac{\kappa \sinh(\alpha l)}{\alpha} & \cosh(\alpha l) - \dfrac{j\delta \sinh(\alpha l)}{\alpha} \end{bmatrix}, \tag{5}$$

where $\alpha = \sqrt{|\kappa|^2 - \delta^2}$ and $\kappa = \dfrac{\pi n_1 \Gamma}{\lambda}$, where n_1 and Γ are the magnitude of the refractive index perturbation and the fraction of the power propagating in the core of the optical fiber, respectively. Solving the linear system of Eq. (4), the reflectance of the FBG is then given directly by the transfer matrix components

$$R(\lambda) = \left|\frac{E_r(0)}{E_i(0)}\right|^2 = \left|\frac{T_{21}(\lambda)}{T_{11}(\lambda)}\right|^2. \tag{6}$$

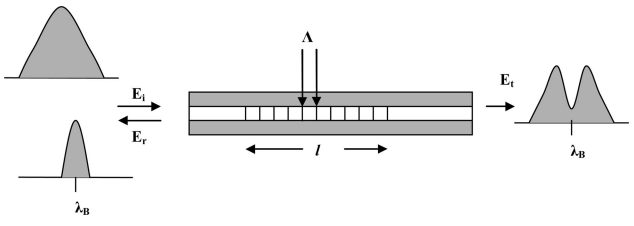

Fig. 1. Model of a reflective-type FBG illuminated by a broadband source or scanned by a tunable laser; most of the incident beam is transmitted, but a narrow band with a center wavelength (Bragg wavelength) at λ_B is reflected in the direction of the source. The center wavelength is directly related to the period of the FBG and the effective refractive index.

B. FBGA and C-OFDR

In the C-OFDR system, a coherent source scans the FBGA as a function of wavelength as shown in Fig. 2. Physically, the reflections from each FBG in the array interfere with the reflection from the reference reflector. The net effect is a composite modulation of the FBGs, where beat frequencies of the modulation are

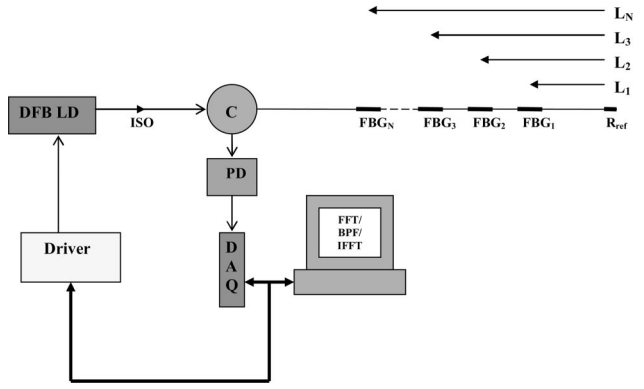

Fig. 2. Block diagram of a FBGA with C-OFDR interrogation. The tunable laser wavelength scans an optical fiber line composed of an N-element FBGA and a reference reflector, resulting in a modulated interferometric signal. The modulated interferometric signal is detected by a photo-optic detector, and by using a Fourier transform, a bandpass filter, and an inverse Fourier transform, the positional and wavelength information of a desired FBG are determined.

directly related to the position of the FBGs with respect to the reference reflector. There are also interferences between the FBGs resulting in cavity interferences. Taking the Fourier transform of the FBGA system signal spatially separates out each FBG in the array. A bandpass filter, centered on a particular beat frequency, is then used to extract the corresponding FBG signal from the Fourier transform. This is followed by an inverse Fourier transform to recover the FBG spectrum. The reflector position is slightly different from the design used by Childers *et al.*[3]; the reflector is positioned at the tip of the optical fiber instead of between the source and the FBGA. The primary advantage of positioning the reflector at the tip is that there will be no breaks in the fiber to create the reflector; this makes it desirable from a manufacturing point of view. Also, the Fresnel reflection at the tip can be used as the reflector; thus no further step is necessary other than properly cleaving the optical fiber. This has the added advantage in that the beat frequencies can be controlled by properly positioning and cleaving the tip of the fiber.

The transfer matrix approach can be used to model the FBGA system as shown in Fig. 3, similar to the arrangement shown in the previous section for the FBG. The transfer matrix $\mathbf{T}$ can be considered as a multiplication of individual FBGs, reflector, $\mathbf{R_{ref}}$, and phase, $\mathbf{P}$, transfer matrices. For a FBGA with a Fresnel reflector at the tip, the transfer matrix of the FBGA system is given by

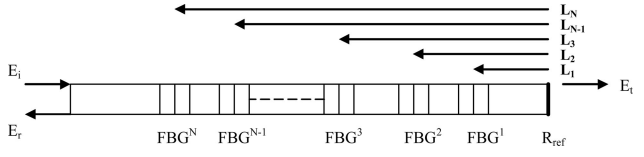

Fig. 3. Model of an N-element FBGA with a backend reference reflector.

$$T = [R_{ref}][P]\lfloor \mathrm{FBG}^1 \rfloor [P]\lfloor \mathrm{FBG}^2 \rfloor [P]\lfloor \mathrm{FBG}^3 \rfloor \ldots \times \lfloor \mathrm{FBG}^{N-1} \rfloor [P]\lfloor \mathrm{FBG}^N \rfloor, \quad (7)$$

where

$$\mathbf{P} = \exp\begin{bmatrix} -\frac{4\pi n}{\lambda} l_p & 0 \\ 0 & \frac{4\pi n}{\lambda} l_p \end{bmatrix}, \quad (8)$$

$$\mathbf{R_{ref}} = \frac{1}{t}\begin{bmatrix} r & 0 \\ 0 & -r \end{bmatrix}, \quad (9)$$

$$r = \frac{n-1}{n+1}, \quad (10)$$

$$t = \frac{2n}{n+1}, \quad (11)$$

where l_p, r, and t are the separation length between the FBGs, the Fresnel reflectivity, and the Fresnel transmissivity of the reflector, respectively.[7] The FBGs are all identical where the transfer matrix is given by Eq. (5). The resulting transfer matrix and reflectance of the FBGA system are then given by Eqs. (7) and (6), respectively. In a double-pass configuration, the beat frequencies produced by the interference between the FBGs and the reference reflector are directly related to the relative position (L_i) of the individual FBGs with respect to the reference reflector:

$$f_i = \frac{2nL_i}{\lambda^2}. \quad (12)$$

In addition to the interference between the FBGs and the reflector, there are also interferences between the FBGs, resulting in cavity interferences. The resulting beat frequency produced by the cavity interference is then given by

$$f_{ij} = \frac{2n|L_i - L_j|}{\lambda^2}. \quad (13)$$

Furthermore, higher-order interferences can result from a multiple pass through the system and interferences between the beats. To recover the individual FBG spectrum using a C-OFDR, the Fourier transform of the FBGA reflectance spectrum is taken. A simple bandpass filter, represented by a rectangular window (REC) of width W and centered at a desired beat frequency (f_i), is then used to extract the desired FBG signal from the Fourier spectrum. Once extracted, this information is then inverse Fourier transformed to recover the wavelength information of the desired FBG or in a mathematical form given by

$$\mathrm{FBG}_i(\lambda) = \left| F^{-1}\left\{ F(R(\lambda))\mathrm{REC}\left(\frac{f - f_i}{W}\right)\right\}\right|,$$

$$\mathrm{REC}(x) = \begin{cases} 1 & |x| \le \frac{1}{2} \\ 0 & \text{otherwise} \end{cases}, \tag{14}$$

where $F(\,)$ and $F^{-1}(\,)$ are the Fourier and inverse Fourier transform, respectively. The required bandwidth of the bandpass filter is inversely related to the wavelength bandwidth of the FBGs:

$$W \ge \frac{1}{\Delta\lambda}. \tag{15}$$

For a low-reflectance FBG, the wavelength bandwidth is directly given by the free spectral range and the effective refractive index:

$$\Delta\lambda = \frac{\lambda^2}{2nl}. \tag{16}$$

It is possible for the cavity interferences to superimpose onto FBG-reflector interferences when their corresponding beat frequencies are equal, $f_i = f_{ij}$, resulting in distortion of the recovered FBG spectra. Several techniques have been implemented to eliminate this distortion. The first technique is to reduce the reflectance of the FBGs to a level that minimizes the cavity interferences. The second method is to downshift the cavity interferences to a lower-frequency band such that $L_1 > |L_N - L_1|$.[5] A third technique, simulated in a prior paper, is to actively subtract the cavity interferences directly from the overall FGBA system interference signal.[4] A fourth technique is to design the FBGA system such that the cavity interferences and the FBG-reflector interferences do not overlap. The latter is the technique used in this work.

C. Strain-Optic Relationship

The Bragg wavelength of a FBG is directly related to the period (Λ) of the grating and the effective refractive index as shown in Eq. (3). Changes in the period and/or the effective refractive index of the FBG will change the Bragg wavelength; the changes can be attributable to mechanical and/or temperature perturbations. The optical response of a FBG because of changes in temperature and strain is given by[8]

$$\frac{\Delta\lambda_B}{\lambda_B} = \mathrm{SGF}\Delta\varepsilon + \mathrm{TGF}\Delta T, \tag{17}$$

where $\Delta\lambda_B$, TGF, and SGF are the changes in the center wavelength of the FBG, the temperature gauge factor, and the strain gauge factor, respectively. In this paper, we are concerned only with the SGF. The SGF is directly related to the photoelectric coefficient, ρ_{ij}, and the Poisson ratio, ν, of the fiber[8]

$$\mathrm{SGF} = 1 - \frac{n^2}{2}[\rho_{12} - \nu(\rho_{11} + \rho_{12})]. \tag{18}$$

For the case of fused-silica glass, where $\rho_{11} = 0.121$, $\rho_{12} = 0.270$, $\nu = 0.17$, and $n = 1.458$, the SGF is 0.78. Previous research has shown that the SGF for a FBG fabricated from a standard or germanium–boron codoped optical fiber is closer to 0.8.[9] The SGF was determined experimentally for a germanium–boron codoped fiber used in this work.

3. C-OFDR and FBGA Design

A. Simulation Software

MATLAB-based software was previously developed to simulate the FBGA–C-OFDR system using transfer matrices.[10] Further developments were made to create a layout graphical user interface (GUI), where the devices can be assembled in an object-oriented fashion. Figure 4 shows the software used. The user can

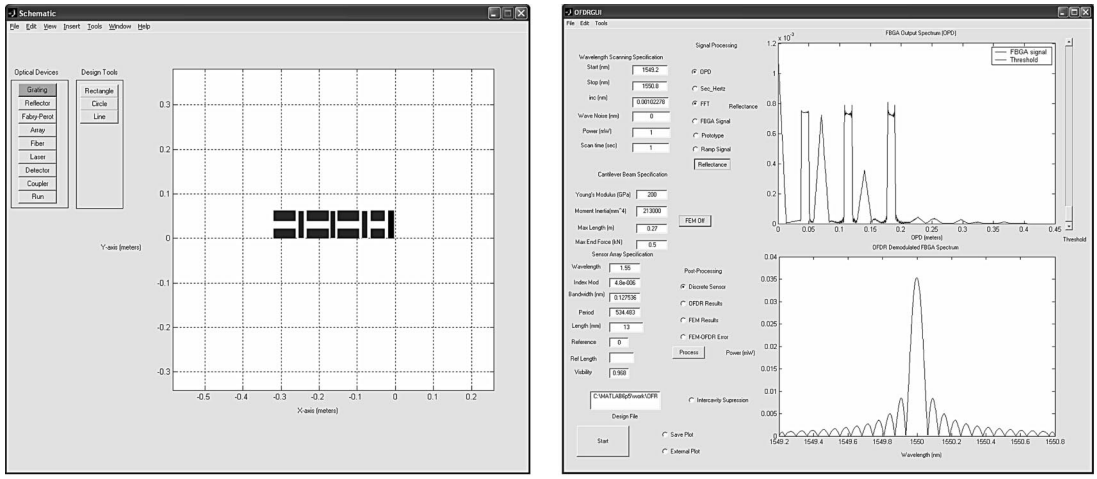

(a) **(b)**

Fig. 4. Simulation software used to model the FBGA system. (a) The FBGA system is designed on the layout GUI, and (b) the analysis is done on the processor GUI.

place and position the devices on the GUI layout in the desired order and with a click input the desired device geometry and optical characteristics. The parameters are then stored in a file. The processor will then read the parameter file and look up the transfer matrix of each device on the layout and then input the device parameters into the proper transfer matrix. The final transfer matrix is then assembled in the order given in the layout, and the resulting reflectance of the system is determined. A Fourier transform is then performed on the reflectance spectrum. The cursors are used to band a particular FBG in the Fourier spectrum and extract the FBG signal. An inverse Fourier transform is then performed on the extracted signal to recover the FBG reflectance spectrum. Each step in the process is seen visually through several plotting routines. The simulation software also has the ability to process raw experimental FBGA signals; thus, the experimental and simulation results can be compared directly.

B. FBGA Design and Simulation

The Tunics-BT tunable laser has a minimum wavelength increment of 1 pm and a repeatability of ± 5 pm. From the specification data sheet of the tunable laser, mode hopping and wavelength drifts attributable to temperature are compensated. The optical path difference that corresponds to 1 pm period is 83 cm at 1550 μm using the free-spectral-range equation and a refractive index of 1.45. The maximum possible length of the FBGA system is 41.5 cm using the Nyquist criteria. In the Nyquist criteria, a waveform is reproduced exactly if the sampling rate is twice the highest frequency component of the waveform. To be conservative, the length of the FBGA system was set at 20.8 cm or one half the maximum length, a safety factor of 2. The length of the FBGA was chosen to be approximately 15 cm, allowing a 5.8 cm margin to optimize the position of the reference reflector. The criterion for the optimum position of the reflector is such that cavity interferences do not overlap with the FBG-reflector interferences. The maximum number of FBGs possible for a 15 cm FBGA is limited by cavity interferences and the width of each FBG. The phase mask used allowed a maximum length of 1.3 cm for the FBG; as a matter of convenience a three-element FBGA was the best choice, although the number can be increased by re-

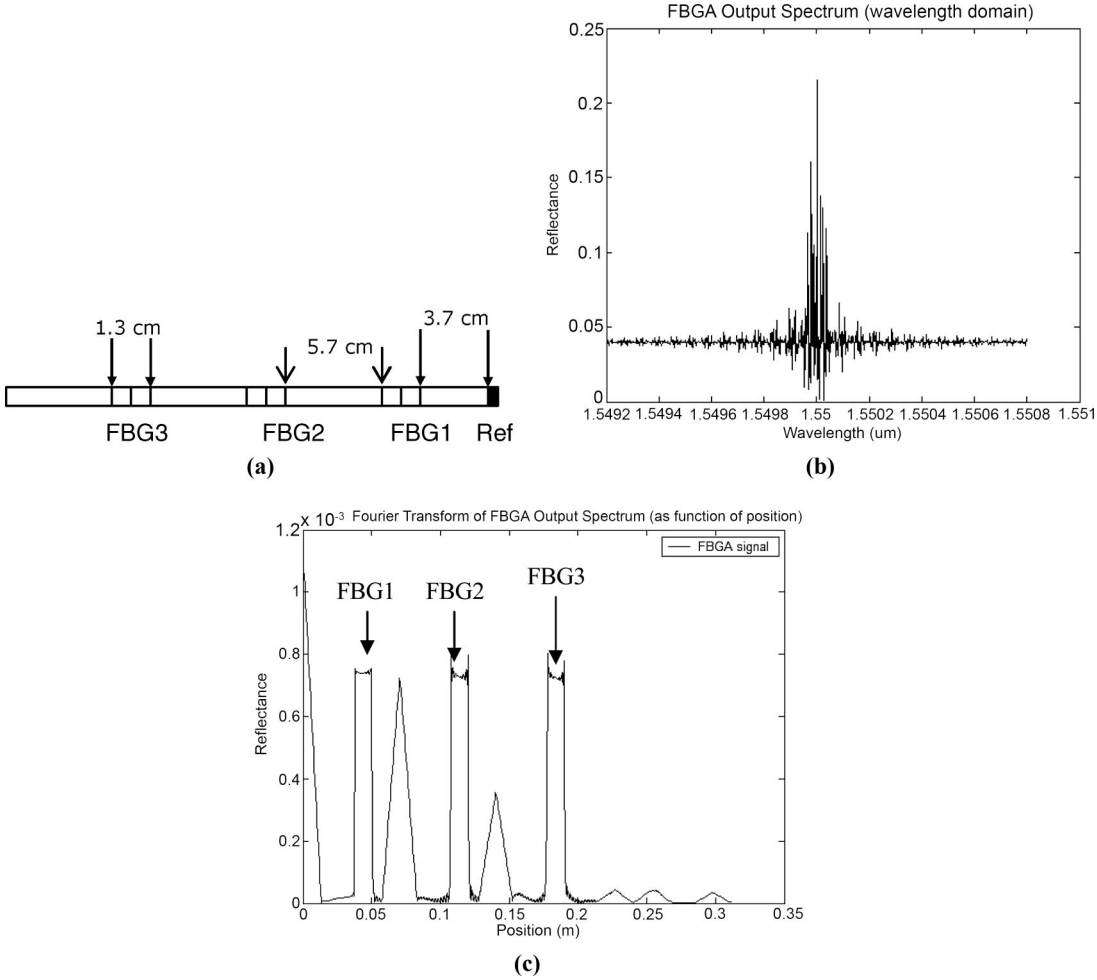

Fig. 5. Design of the three-element, 15.3 cm FBGA, and the resulting interferometric signal in (a) the Fourier domain and (b) the wavelength domain. The operating bandwidth is 1.6 nm, and the tunable laser wavelength increment is 1 pm.

ducing the length of the FBGs. The software program was used to determine the optimum reflectance for the FBGs in the array and the reference reflector position. It was determined that the optimum position of the reflector was between 2 and 4 cm from the FBGA to prevent an overlap. The reflectance of each FBG in the array was set at 1% with a 4% Fresnel reflectance for the reference reflector at the tip of the fiber. The reflectance of the FBGs was chosen so that the FBG-reflector interferences were comparable or larger in magnitude than the cavity interferences. However, this is not critical since the cavity interferences and the FBG-reflector interferences in the final design do not overlap. Figure 5(a) shows the final design layout. The final length of the FBGA is 15.3 cm and contains three FBGs 1.3 cm wide and 128 pm in bandwidth. Each FBG is separated by 5.5 cm with the reflectance reflector positioned 3.7 cm from the FBGA. Figures 5(b) and 5(c) show the resulting interference signals from the FBGA system in the wavelength and Fourier domain. The range of the Fourier transform shown in Fig. 5(c) is with respect to the reference reflector position. The first, third, and fifth peaks in Fig. 5(c) are the FBG-reflector interferences, and the second and the fourth peaks are the cavity interferences; the rest of the interference peaks are higher-order interferences. As shown in Fig. 5, the cavity interferences and FBG-reflector interferences are separated in the Fourier domain; this satisfies the main design criteria.

4. FBGA System Fabrication

The final design of the FBGA from Section 3 was copied onto a piece of paper, and the position of each FBG was marked along the photosensitive fiber. The optical fiber used was a boron–germanium codoped photosensitive fiber, F-SBG-15, from Newport Corp., and operating at 1550 nm. Photosensitive fibers require less energy and exposure time to make FBGs compared with standard optical fibers and can produce highly reflective FBGs without the need for hydrogen loading.[6,7]

A striper was then used to remove 2.5 cm of the coating around the position of each FBG. The FBGs were inscribed into the core of the photosensitive fiber using the phase mask technique, where the period of the phase mask was 1072 nm. The writing source was a frequency-doubled cw argon-ion laser operating at 244 nm (UV). By controlling the tension of the optical fiber and monitoring the back reflectivity using an erbium-doped fiber amplifier (EDFA) source and an optical spectrum analyzer (OSA), each FBG in the array was given a similar peak wavelength and reflectance of ~1551.2 nm and ~1%, respectively. The bandwidth of each FBG is approximately 120 pm. In addition to the FBGA system, a single 1.3 cm FBG, with a reflectance of 0.9 and a bandwidth of 200 pm, was also fabricated using the same procedure as above; it was used for the purpose of determining the SGF of the FBG.

5. Fiber Bragg Grating Calibration

A. Fabry–Perot Interferometric Displacement and Strain Sensor

A Fabry–Perot interferometer (FPI) is a multiple-beam-interference optical device that is composed of two semireflective mirrors separated by a cavity.[11] In this work we are interested in using a fiber-optic FPI as a displacement and strain measurement device as shown in Fig. 6. R_1 is the reflectance from the front end of a cleaved single-mode optical fiber, and R_2 is the reflectance from a position that is adjustable. In this section, R_1 and R_2 will also be used to label the reflecting surfaces. One end of a test sensor is attached to surface R_2, and the other end of the test sensor is kept fixed. The optical field reflects from both end faces and interferes; assuming the cavity is filled with air, the round-trip phase is given by

$$\phi = \frac{4\pi(l - \Delta l)}{\lambda} = kz_0, \tag{19}$$

where l, Δl, z_0, and $k = 2\pi/\lambda$ are the nominal cavity length, cavity displacement, round-trip path length, and propagation constant, respectively. For the case of the fiber-optic FPI displacement sensor shown in Fig. 6, the optical field will diffract over the length of the cavity. Assuming Gaussian approximation for the LP_{01} mode propagating in the single-mode fiber, the fraction of the optical power re-entering the single-mode optical fiber is given by the transmission or coupling coefficient[12]:

$$T(z_0) = \left(1 + \frac{{z_0}^2\lambda^2}{4\pi^2{w_0}^4}\right)^{-1}. \tag{20}$$

Equation (20) assumes only longitudinal misalignment between surface R_1 and surface R_2. In this work the operating wavelength was 1542.9 nm; the tip of the optical fiber was cleaved giving a Fresnel reflectance of 4%; the material of surface R_2 was aluminum with 70% reflectance at 1550 nm. A single-mode SMF28 step-index optical fiber, with a mode field radius of 5.2 μm at 1550 nm, was used. Entering the

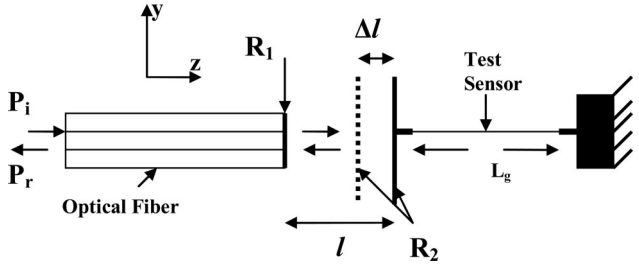

Fig. 6. Fiber-optic FPI displacement and strain sensor. R_1 is the reflectance from the front end of an optical fiber, and R_2 is the reflectance from a position that is adjustable. The optical field reflects from both end faces and interferes. One end of a test sensor is attached to surface R_2, while the other end is fixed. The displacement of surface R_2 strains the test sensor.

required parameters for Eq. (20), the transmittance drops below 6% for cavity lengths longer than 250 μm. Since the reflectance of R_1 and the transmittance are below 10%, the two-beam interference method can be used to approximate the resultant field just to the left of the surface R_1. The resultant field is the sum of the field reflecting from surface R_1 and the field contribution from surface R_2. The reflectance of the FPI displacement sensor is then given by[13]

$$\frac{P_r}{P_i} \approx R_1 + (1-R_1)^2 R_2 T(z_0) + 2\sqrt{R_1 R_2 T(z_0)} \times (1-R_1)\cos(\phi). \quad (21)$$

The contrast of the FPI signal is then given by

$$\nu = \frac{2\sqrt{R_1 R_2 T(z_0)}(1-R_1)}{R_1 + (1-R_1)^2 R_2 T(z_0)}. \quad (22)$$

The contrast is 100% at the 250 μm cavity length; at this position, the field contribution from surface R_2 matches the field contribution from surface R_1; thus, the reflectance of the FPI can be further reduced to

$$\frac{P_r}{P_i} \approx 2R_1(1+\cos\phi). \quad (23)$$

Ideally, 250 μm is the optimum cavity length for the parameters given because the fringes will be most pronounced, and their magnitude will essentially remain constant. However, the optimum cavity length will depend on the quality of the reflecting surfaces, scattering effects, surface alignments, and polarization. As shown in Fig. 6, the resulting strain in the test sensor owing to a displacement Δl is then given by

$$\varepsilon = \frac{\Delta l}{L_g} = N\frac{\lambda}{2L_g}, \quad (24)$$

where L_g and N are the gauge length and the corresponding number of observed fringes, respectively.

B. Fabry–Perot Interferometric Strain Gauge Calibrator

The FPI strain gauge calibrator setup is shown in Fig. 7. The main impetus for fabricating the FPI strain gauge calibrator was to test strain sensors in a nondestructive fashion. The setup is composed of four main components: the rail, two sensor holders, the piezoelectric actuator, and a FPI displacement sensor. The rail was used to adjust the gauge length, L_g, by varying the relative position of the sensor holders. The rail was fabricated from a single aluminum block with dimensions of 18 cm × 3.7 cm × 2 cm. The aluminum sensor holders hold both ends of the test sensor. On one sensor holder (SH#2) is a tensioner that keeps one end of the test sensor fixed by friction adjusted with a side screw. The second holder (SH#1) is attached to the piezoelectric actuator through a 2 mm diameter cemented machine screw. The piezoelectric actuator used was fabricated with a 2.7 cm diameter piezoceramic transducer, Radio-Shack model 273-0373A. The outer edge of the piezoelectric actuator was cemented to an aluminum block (piezo housing) with dimensions of 4 cm × 4 cm × 0.5 cm and with a 2.5 cm diameter clear hole. SH#1 and SH#2 are composed of a lower and an upper half. The lower half slides on the aluminum rail, while the upper half clamps the test sensor in place. The dimensions of the lower half of SH#1 are 2.5 cm × 2 cm × 0.52 cm, and the upper half has dimensions of 1 cm × 2 cm × 0.2 cm. The dimensions of the lower half of SH#2 are similar to those of SH#1; however, the length of the lower half is 2 cm longer to provide more clearance for sensor leads. To prevent the sensor holders from damaging the sensors, two thin layers of plastic were glued between the upper and lower parts. Two machine screws were then used to tightly grip the test sensor to the sensor holders. A low-finesse FPI was set up between a cleaved tip of a single-mode SMF 28 optical fiber and the machine finished surface of SH#1. The FPI is held in place between two aluminum blocks (FPI holder) with dimensions of 3.7 cm × 1 cm × 0.3 cm and 2 cm × 1 cm × 0.3 cm, respectively. A small groove was machined onto the lower FPI holder to properly align the cleaved end of the optical fiber. Two thin layers of plastic were used to prevent damage to the optical fiber, similar to the SH#1 and SH#2 arrangements. Two machine screws were then used to tighten the FPI holder.

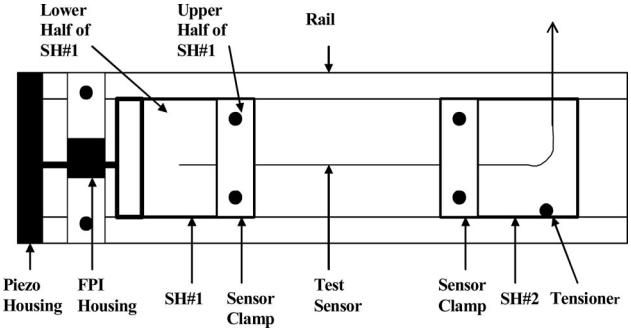

Fig. 7. Physical layout of the FPI strain gauge calibrator. The system is composed of two sensor holders (SH#1 and SH#2) positioned on a groove. SH#2 is kept fixed by friction using an adjustable side screw (tensioner). The test sensor is kept in tension and fixed by SH#1 and SH#2. The FPI displacement sensor is composed of a cleaved front facet of a SMF28 optical fiber and the machine-finished surface of SH#1. The piezoceramic housing (piezo housing) fixes the outer edges of the piezoceramic actuator.

C. Strain Gauge Factor for a Fiber Bragg Grating

The setup in Fig. 8 was used to determine the SGF of the FBG strain sensor. An EDFA source was used to source the FBG, and the reflectance spectrum was observed on an OSA. The gauge length for the FPI strain gauge calibrator was set at 8 cm, and the FPI was sourced by a diode laser operating at 1542.9 nm. Using the operating wavelength and the gauge length, the conversion factor between the strain and the number of fringes was determined to be 9.64 με per fringe. The high-voltage source was manually ramped in four stages corresponding to 4, 8, 12, and

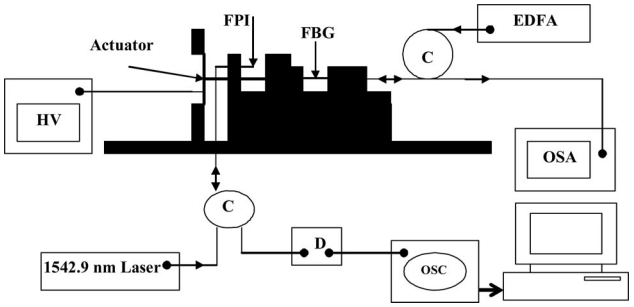

Fig. 8. Hardware setup used to measure the strain gauge factor of a FBG. The setup includes couplers (C), a high-voltage source (HV), an erbium-doped fiber amplifier (EDFA) broadband source, a fiber-optic photodetector (PD), a computer-based oscilloscope (OSC), and an optical spectrum analyzer (OSA).

16 fringe spacings, with each stage starting from the initial position. The entire measurement procedure was repeated three times for average values. The fractional change in the Bragg wavelength was determined by dividing the change in the Bragg wavelength by the Bragg wavelength. Figure 9(a) shows the average and standard deviations of the fraction change in Bragg wavelength as a function of strain. A linear fit of the data points is also shown; from the slope of the fit, the SGF is 0.77.

To confirm the results above for the SGF, the FBG was bonded to a 75 cm $\times$ 3 cm $\times$ 0.2 cm aluminum cantilever beam using epoxy, along with an electric strain gauge (ESG). The ESG used is of the resistive type, model CEA-06-250UN-120, with a SGF of 2.085; the gauge length is 6.35 mm, and the matrix length is 13.2 mm. A 30 cm measuring ruler located at the tip end was used to determine the vertical displacement of the beam. A quarter-Wheatstone bridge/amplifier and a digital voltmeter (DVM) arrangement were used to interrogate the ESG. The tip of the cantilever beam was displaced by 12 cm in increments of 1 cm. The change in the Bragg wavelength as observed on the OSA was then correlated with axial strain information from the ESG. Figure 9(b) shows the fractional change in Bragg wavelength as a function of strain. A fit was then taken between the fractional change in the Bragg wavelength and the measured strain. The slope of the fit gives a SGF of 0.75, confirming the results using the Fabry–Perot strain gauge calibrator. The added advantage of the FPI strain gauge calibrator is that it is nondestructive and the FBG can be reused after the calibration.

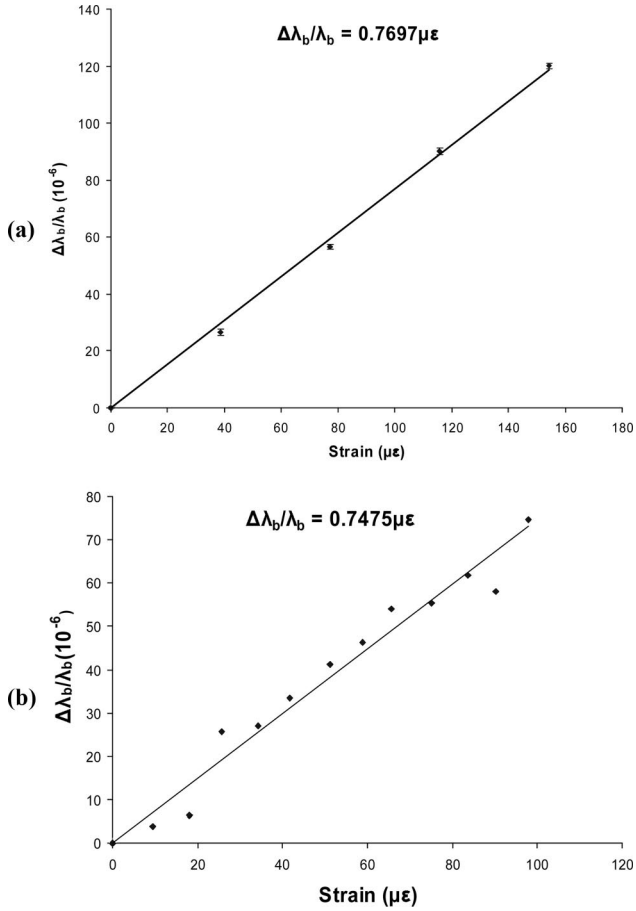

Fig. 10. Fractional change of the center wavelength of the FBG as a function of induced strain using (a) the FPI strain gauge calibrator and (b) the cantilever beam method. Note that the fits are forced to cross the origin.

6. FBGA and C-OFDR Testing

A. FBGA/OFDR and Cantilever Beam Host

The three-element, 15 cm FBGA was bonded to the 75 cm $\times$ 3 cm $\times$ 0.2 cm aluminum cantilever beam

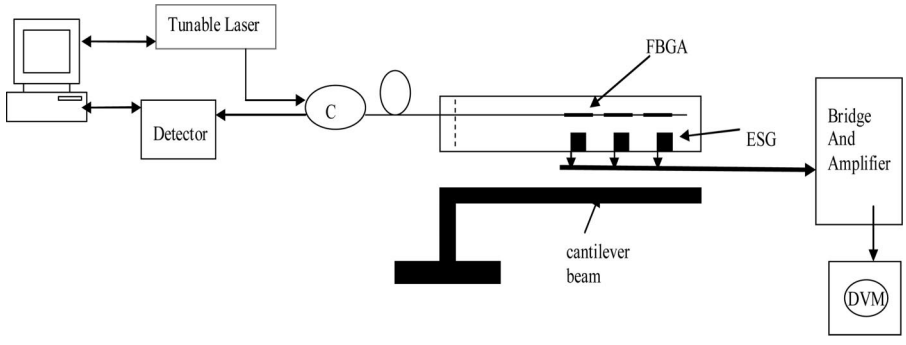

Fig. 9. FBGA and ESG attachment to a cantilever beam host. The tip of the cantilever beam is varied, and the corresponding strain information from the FBGs and ESGs are compared.

by using epoxy. Three ESG gauges (CEA-06-250UN-120) were located next to the position of each FBG in the array. A 30 cm measuring ruler located at the tip end was used to determine the vertical displacement of the beam. A tunable laser diode (Tunics-BT) was used to source the FBGA, and a bridge/amplifier arrangement was used to interrogate the ESG. Figure 10 shows the layout. The resulting signal from the amplifier was then measured using a DVM. Both the tunable laser and the fiber-optic photodetector were controlled through the computer (PC) using a general-purpose interface bus.

B. C-OFDR and FBGA Results

The setup in Fig. 10 was used to test the FBGA. The tip of the cantilever beam was displaced by 5, 10, and 15 cm. At each displacement, the signal from the bridge/amplifier was measured for each ESG. Following the ESG measurements, the signal from the FBGA system was recorded. The simulation software was then used to process the raw FBGA system signal. The signal was Fourier transformed and the three FBG-reflector interference peaks extracted. To recover the spectrum for each FBG in the array, the extracted peaks are then inverse Fourier transformed. From this, the changes in the Bragg wavelength were recorded for each FBG as the tip of the cantilever beam was displaced by 5, 10, and 15 cm. Figures 11(a) and 11(b) show the FBGA interference signal in the wavelength and Fourier domains. Figure 11(c) shows the demodulated spectrum for each FBG at 0 and 15 cm cantilever tip displacement. Figure 12 shows the ESG results and the measured strain at each position of the FBG at various displacement points of the cantilever beam. The trend shown in Fig. 12 is what is expected for a rectangular cantilever beam. For a rectangular cantilever beam, the clamped end has the largest axial strain, and the tip of the cantilever beam has the lowest axial strain; between the two extremes is a linear relationship between the position and the strain. In addition, the magnitude of the axial strain is directly related to the tip displacement; this will tend to shift the entire strain field upward as the tip displacement increases as shown in Fig. 12. From Fig. 12, the peak strain is approximately 140 $\mu\varepsilon$, and the peak percent strain error with respect to the ESG results is 18.5%. The ESG and FBGA results were comparable as shown in Fig. 12. The differences can be attributed to the quality of the bonding of the FBGA and ESG to the cantilever beam. There are also errors when the peaks are extracted and inverse Fourier transformed to get the FBG spectrum. Depending on the width of the rectangular window, the recovered spectrum shape

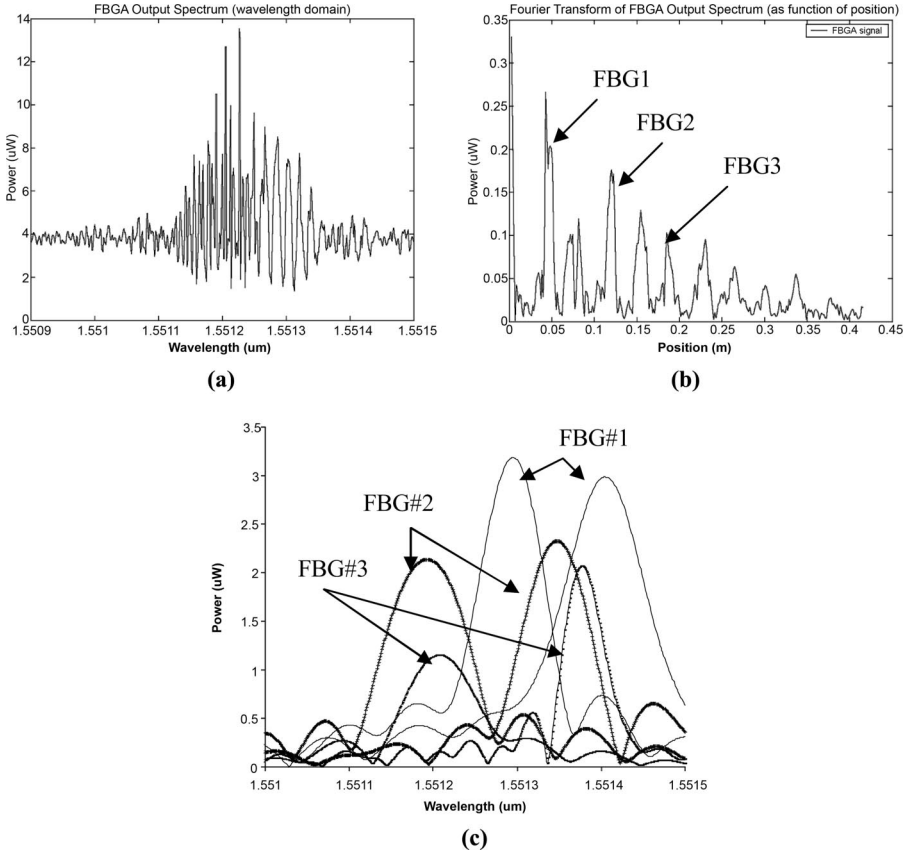

Fig. 11. FBGA reflectance spectrum in the (a) wavelength and (b) Fourier domains. Note the decrease in the magnitude of the interference peaks as a function of position. (c) FBGA demodulated spectrum. Note the decrease in the peak magnitude and the distortion of the FBG spectra, particularly for FBG3.

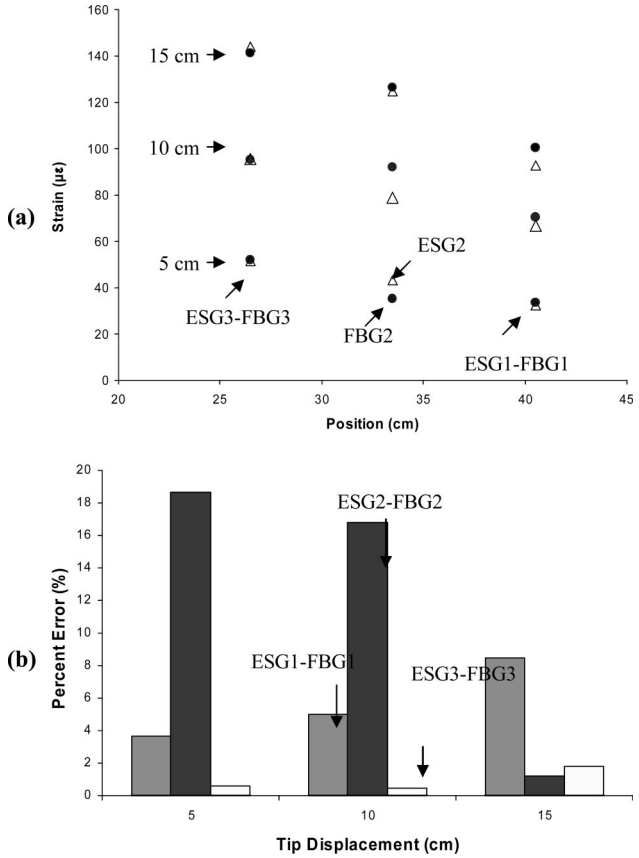

Fig. 12. (a) ESG and FBGA results as functions of cantilever beam tip displacement and axial position. (b) Percent strain error of each FBG in the array with respect to the ESG results as functions of tip displacement.

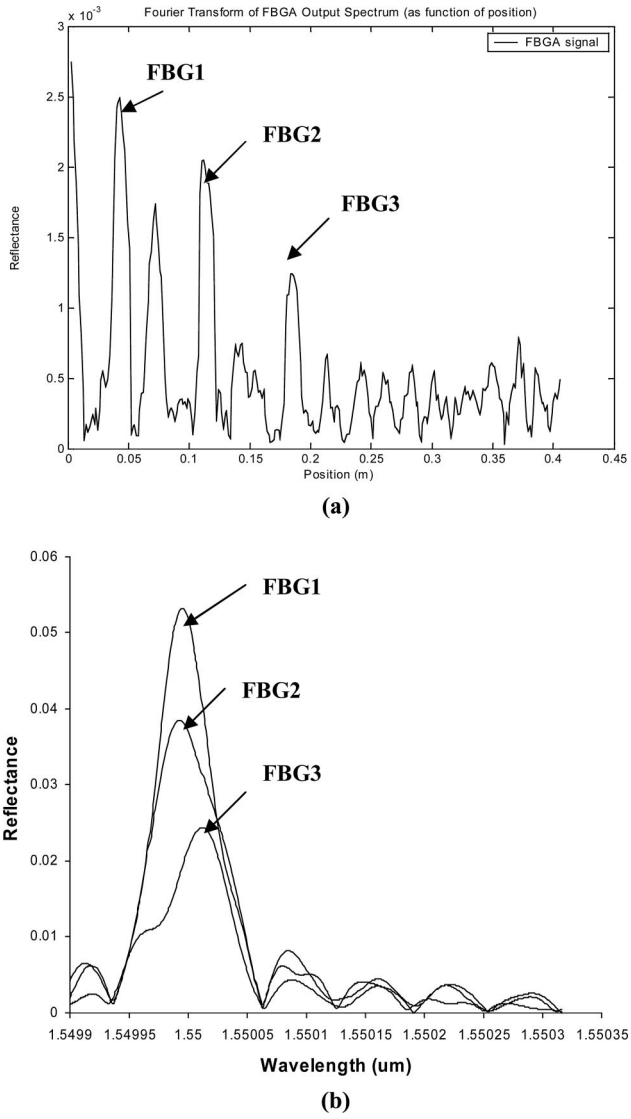

Fig. 13. Simulated FBGA reflectance in (a) the Fourier domain with a 2.5 pm uniform noise added to the wavelength increment. Note the decrease in the magnitude of the interference peaks as a function of position. (b) FBGA demodulated spectrum. Note the decrease in the peak magnitude and the distortion of the FBG spectra, particularly for FBG3.

can vary resulting in slight variations in the center wavelength. Also, the repeatability of the laser introduces error in the FBGA strain measurements; if the worst case is taken, a repeatability of ± 5 pm will translate to ± 4 $\mu\varepsilon$ error.

7. Discussion

The simulated and experiment FBGA Fourier spectrum gave similar positioning of the interference peaks, including the higher-order interferences. However, in the experimental data, the magnitude of the interference peaks decreases as a function of position. In addition to a decrease in the magnitude of the interference peaks, the demodulated FBGA system signal shows a distortion of the recovered FBG spectra; FBG3 shows the largest effect. This suggests an error in the wavelength increment at the 1 pm setting attributable to the tuning mechanism of the laser; this makes sense since the repeatability of the laser is ± 5 pm. To confirm this hypothesis, the simulation done in Subsection 3.B was repeated but this time adding a 2.5 pm uniform random wavelength noise on top of the 1 pm wavelength increment. Adding 2.5 pm noise to the wavelength increment means that the minimum wavelength increment is 1 pm, and the maximum wavelength increment is 3.5 pm. Figure 13 shows the results. In the figure, the magnitude of the interference peaks decreases as a function of position, similar to the experimental data. Also, the recovered FBG spectra show a drop in their peak magnitude and distortion of the spectrum, particularly for FBG3, similar to the experiment. It took several runs to get the results shown in Fig. 13, suggesting that the laser tuning mechanism is not a pure white-noise distribution; in fact, the trend in the experimental data is consistent over several runs, suggesting an additional component inherent to the tuning mechanism of the laser. However, from the simulation results, we can conclude that the tunable laser has nonuniform wavelength-stepping increments at the 1 pm setting. To take a direct Fourier transform of the FBGA system signal, naturally, the

sampling of the FBGA system signal has to be uniform or erroneous results will occur in the Fourier domain. To take into account the ±5 pm repeatability of the tunable laser, the maximum FBGA system length should be set at 8 cm. The effects of the variation of the wavelength in a C-OFDR system have been observed by others, and reducing its effect is a current research topic.[14] Typically, if the tuning is continuous and not incremental, the variation in the wavelength can be minimized by coupling a reference interferometer to the tunable laser.[5] The resulting interference from the reference interferometer has precise spacing as was shown in the analysis of the FPI. The length of the interferometer must be greater than twice the length of the FBGA system to satisfy the Nyquist criteria. The previous techniques used to investigate the stepping accuracy of the tunable laser suggest a way to determine the tuning quality of a tunable laser. For example, if a FBGA system designed to work at 1 pm is used, then the magnitude of the FBG-reflector interference peaks should be flat at the 1 pm wavelength setting of the tunable laser.

Using an incremental tunable laser has several disadvantages. The time to make an entire scan was long, typically requiring 5 min at increments of 1 pm, therefore, dynamic measurements were out of the question using our setup. Also, owing to the finite stepping wavelength increment of the tunable laser, the maximum length of the FBGA was limited as was shown in this work. In the final FBGA design, the FBGs in the array are also spaced too closely to be of a practical use. It makes more sense for each FBG to measure different parameters, for example, one FBG can measure strain, while the other two can measure temperature and pressure, respectively. To achieve a longer FBGA and/or faster measurements, a continuous-scan tunable laser is required, for example, a fast tunable fiber laser system. If the measurement speed is increased, then each FBG in the array can be calibrated using the FPI strain gauge calibrator. Each FBG in the array would then experience the same strain field; this will make it possible to simultaneously calibrate all the FBGs. Sidney *et al.*[15] demonstrated the calibration of a FBG using C-OFDR interrogation. Instead of using the EDFA, C-OFDR can be used to interrogate the FBGA system. This will eliminate the cantilever beam for testing purposes, and the FBGA can be used after calibration and testing.

8. Conclusion

We have shown that the transfer matrix approach can be used to model a FBGA–C-OFDR system. In this approach, an elemental transfer matrix is used to represent the optical and geometrical characteristics of a single element in the FBGA system. The response of the entire FBGA system can then be determined simply by multiplying all the elemental transfer matrices in the proper order. The advantage of this approach is that any optical device can efficiently be incorporated if its transfer matrix is known. We have successfully used this approach to design and simulate a 15.3 cm, three-element fiber Bragg grating array with the optical frequency domain reflectometry interrogation technique. A comparison between the simulation and experimental findings showed that the simulation and experimental results gave similar positional information of the FBGs; however, in the experimental data, the magnitude of the interference peaks decreased as a function of FBG position. In addition, the recovered FBG spectra showed a drop in peak magnitudes and distortion of the FBG spectra. We were able to reproduce this effect in the simulation by the injection of white noise into the wavelength scan. From the simulation results, we conclude that the tunable laser had nonuniform variations in the wavelength increments. The recovered FBG spectra were usable, and we were able to perform strain tests on a cantilever beam. The results showed that the peak strain error was 18% compared to the electric strain gauges. Overall, the transfer matrix technique gave an accurate representation of the experimental results and allowed a direct comparison between the experimental and the simulation results. Improvements in measurement speed can be made by employing a continuous-scanning tunable laser. This would allow one-stop calibration and a testing of the FBGA on the Fabry–Perot strain gauge calibrator described in this work, making the calibration and testing cycle nondestructive.

References

1. M. Froggatt, "Distributed measurement of the complex modulation of a photo-induced Bragg grating in an optical fiber," Appl. Opt. **35,** 5162–5164 (1996).
2. B. A. Childers, T. L. Brown, J. P. Moore, and K. H. Wood, "Recent developments in the application of optical frequency domain reflectometry to distributed Bragg grating sensing," Proc. SPIE **4578,** 19–31 (2002).
3. R. G. Duncan, B. A. Childers, D. K. Gifford, D. E. Petti, A. W. Hickson, and T. L. Brown, "Distributed sensing technique for test article damage detection and monitoring," Proc. SPIE **5050,** 367–375 (2002).
4. A. M. Abdi and A. R. Kost, "Theoretical suppression of cavity interferences in a fiber Bragg grating array interrogated with coherent optical frequency domain reflectometry," Smart Mater. Struct. **15,** 1296–1304 (2006).
5. M. Froggatt and J. Moore, "Distributed measurement of static strain in an optical fiber with multiple Bragg gratings at nominally equal wavelengths," Appl. Opt. **37,** 1741–1746 (1998).
6. A. C. Brooks, M. E. Froggatt, S. G. Allison, T. C. Moore, Sr., D. A. Hare, C. F. Batten, and D. C. Jegley, "Use of 3000 Bragg grating strain sensors distributed on four eight-meter optical fibers during static load tests of a composite structure," Proc. SPIE **4332,** 133–142 (2001).
7. R. Kashyap, *Fiber Bragg Gratings* (Academic, 1996).
8. R. M. Measures, *Structural Monitoring with Fiber Optic Technology* (Academic, 2001).
9. A. T. Alavie, R Maaskant, R. Stubbe, A. Othonos, M. Ohn, B. Sahlgren, and R. M. Measures, "Characterization of fiber Bragg grating sensors and their relation to manufacturing technique," Proc. SPIE **2444,** 528–535 (1995).
10. A. M. Abdi and A. Kost, "Infrastructure optics," Proc. SPIE **5384,** 218–228 (2004).

11. E. Udd, *Fiber Optic Smart Structures* (Wiley, 1995).
12. A. Ghatak and K. Thyagarajan, *Introduction to Fiber Optics* (Cambridge U. Press, 1998).
13. M. del Vries, M. Nasta, V. Bhatia, T. Tran, J. Greene, and R. O. Claus, "Performance of embedded fatigue loaded reinforced concrete specimen," Smart Mater. Struct. **4,** A107–A113 (1995).
14. R. Passy, N. Gision, J. P. von der Weid, and H. Gilgen, "Experimental and theoretical investigations of coherent OFDR with semiconductor laser sources," J. Lightwave Technol. **12,** 1622–1630 (1994).
15. G. A. Sidney, R. L. Fox, M. E. Froggatt, and B. A. Childers, "Novel piezoelectric actuators for tuning an optical fiber Bragg grating," Opt. Eng. **41,** 2448–2455 (2002).